

pubs.acs.org/jasms Research Article

Tackling a Curious Case: Generation of Charge-Tagged Guanosine Radicals by Gas-Phase Electron Transfer and Their Characterization by UV—vis Photodissociation Action Spectroscopy and Theory

Yue Liu, Congcong Ma, Calvin J. A. Leonen, Champak Chatterjee, Gabriela Nováková, Aleš Marek,* and František Tureček*



Cite This: J. Am. Soc. Mass Spectrom. 2021, 32, 772-785



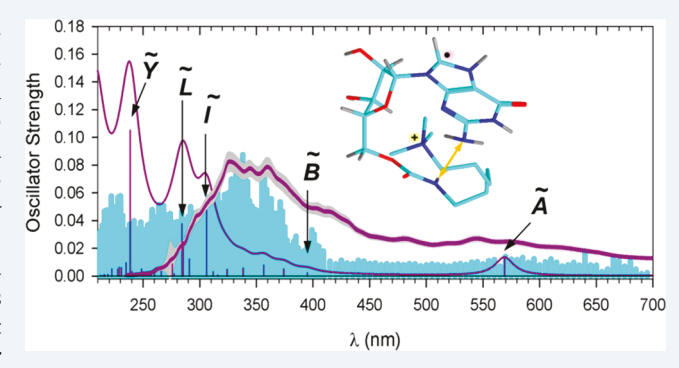
ACCESS

III Metrics & More

Article Recommendations

s Supporting Information

ABSTRACT: We report the generation of gas-phase riboguanosine radicals that were tagged at ribose with a fixed-charge 6-(trimethylammonium)hexane-1-aminocarbonyl group. The radical generation relied on electron transfer from fluoranthene anion to noncovalent dibenzocrown-ether dication complexes which formed nucleoside cation radicals upon one-electron reduction and crownether ligand loss. The cation radicals were characterized by collision-induced dissociation (CID), photodissociation (UVPD), and UV—vis action spectroscopy. Identification of charge-tagged guanosine radicals was challenging because of spontaneous dissociations by loss of a hydrogen atom and guanine that occurred upon storing the ions in the ion trap without further excitation. The loss of H proceeded from an exchangeable position



on N-7 in guanine that was established by deuterium labeling and was the lowest energy dissociation of the guanosine radicals according to transition-state energy calculations. Rate constant measurements revealed an inverse isotope effect on the loss of either hydrogen or deuterium with rate constants $k_{\rm H} = 0.25-0.26~{\rm s}^{-1}$ and $k_{\rm D} = 0.39-0.54~{\rm s}^{-1}$. We used time-dependent density functional theory calculations, including thermal vibronic effects, to predict the absorption spectra of several protomeric radical isomers. The calculated spectra of low-energy N-7-H guanine-radical tautomers closely matched the action spectra. Transition-state-theory calculations of the rate constants for the loss of H-7 and guanine agreed with the experimental rate constants for a narrow range of ion effective temperatures. Our calculations suggest that the observed inverse isotope effect does not arise from the isotope-dependent differences in the transition-state energies. Instead, it may be caused by the dynamics of post-transition-state complexes preceding the product separation.

1. INTRODUCTION

Guanine (G) is the most readily oxidized nucleobase of a low ionization energy (7.85 eV)1 and standard oxidation potential As a result, guanine is readily ionized to a $(0.81-1.58 \text{ V}).^2$ cation radical by electron transfer to another nucleobase cation radical formed by random DNA ionization.^{5,6} In contrast to oxidation, guanine has the largest negative reduction potential among the nucleobases (-2.76 eV), which makes the guanine anion radical extremely reactive toward electron loss and protonation. Regarding electron attachment, the 9-methylguanine-1-methylcytosine anion radical pair has been studied experimentally in the gas phase, and the calculated electron density indicated that the ionizing electron resided in the cytosine ring. The thermodynamics of proton transfer in the guanine-cytosine (C) anion radical pair has been studied by density functional theory (DFT) calculations⁸ that pointed out the role of solvation. Protonation of transient nucleobase anion radicals proceeds rapidly in solution, 4 producing reactive neutral hydrogen atom adducts, such as (G + H)*, which can undergo

further reactions. Our previous computational investigations have indicated that $(G + H)^{\bullet}$ and its 9-methyl derivative are extremely strong bases $(pK_a \sim 20)$ that are expected to undergo fast and complete protonation by solvent or another proton donor. Consistent with this analysis, $(G + H)^{\bullet}$ that was transiently produced in a $(GG + 2H)^{+\bullet}$ dinucleotide by electron transfer in the gas phase underwent fast exothermic intramolecular protonation forming a stable dihydroguanine cation radical. The high reactivity of $(G + H)^{\bullet}$ has so far thwarted attempts to generate it as a stable species for spectroscopic studies. In particular, a UV—vis absorption spectrum of $(G + H)^{\bullet}$

Received: December 13, 2020 Revised: January 27, 2021 Accepted: February 3, 2021 Published: February 10, 2021





Scheme 1. Reaction Sequence for the Generation of Charge-Tagged Guanosine Radicals

$$H_{3}C \oplus CH_{3}$$

$$H_{2}N \oplus H_{3}C \oplus CH_{3}$$

$$H_{3}C \oplus CH_{3}$$

$$H_{3}C \oplus CH_{3}$$

$$H_{4}N \oplus H_{4}N \oplus H$$

is needed to characterize the radical's electronic states for transient monitoring by fast spectroscopy.

We now report that guanosine radicals of the $(G + H)^{\bullet}$ type can be generated as isolated species in the gas phase from conjugates 1+ and 2+ that are tagged with a nonreactive fixedcharge group. This approach is illustrated in Scheme 1 where the fixed-charged tag is a 6-(trimethylammonium)hexane-1-amine group attached via a carbamate linker to O-5' of the ribose moiety. The conjugates are protonated by electrospray ionization (ESI) to form the respective doubly charged ions, $(1 + H)^{2+}$ and $(2 + H)^{2+}$, that are stored in an ion trap and partially discharged by an ion-ion reaction with fluoranthene anion radical.10

Although the electron transfer direction is not specifically controlled in the ion—ion reaction and can result in discharging either positively charged group, reduction of the trimethylammonium group would produce a highly unstable hypervalent ammonium radical of submicrosecond lifetime, 11,12 which is likely to completely dissociate on the experimental time scale of several milliseconds. In contrast, cation radicals of the $(G + H)^{\bullet}$ type, such as $(1 + H)^{+\bullet}$ and $(2 + H)^{+\bullet}$ resulting from electron transfer to the guanidine moiety, are amenable to isolation by mass and further interrogation by tandem mass spectrometry and action spectroscopy.

2. EXPERIMENTAL SECTION

2.1. Materials and Methods. Solvents (methanol, water, acetic acid) of HPLC quality were purchased from Fisher Scientific (Pittsburgh, PA), distilled to remove dissolved sodium, and stored in Pyrex vessels. Deuterated solvents (>99% D content) were purchased from Cambridge Isotope Laboratories (Tewksbury, MA). 2,3:11,12-Dibenzo-18-crown-6-ether

(DBCE) was purchased from Sigma-Aldrich (St. Louis, MO) and used as received. Guanosine conjugate 1+ was synthesized from riboguanosine (Scheme S1), purified by preparative HPLC, and characterized by electrospray and collision-induced dissociation (CID-MS²) mass spectra, as described in the Supporting Information. Conjugate 2⁺ was prepared in situ by deprotection of the 2',3'-O-isopropylidene group with 60/40 trifluoroacetic acid/water for 10 min at room temperature. After evaporation of solvent to dryness, the product was redissolved in 50/50/1 methanol-water-acetic acid and characterized by high-resolution mass spectrometry (Table S1). Mass spectra were measured on a Bruker amaZon Speed 3D ion trap mass spectrometer that was modified for action spectroscopy measurements, as described previously. 13 Collision-induced dissociation (CID) spectra were measured at 0.20 (low excitation amplitude) and 0.40 (high excitation amplitude) instrument power settings. Action spectra were monitored in three wavelength sections, 210-354, 355-409, and 410-700 nm, using two laser pulses, and the laser pulse energies were measured at each experimental wavelength. The photofragment ion intensities were normalized to the number of photons per pulse. The reported spectra were averaged over two runs measured at different days. H/D exchange in $(1^+ + DBCE + H)^{2+}$ and $(2^+ + DBCE + H)^{2+}$ was achieved in a $D_2O/CD_3OD/$ CH₃COOD solution, and the D content in the gas-phase ions was sustained by introducing D2O vapor in the enclosed electrospray volume.

2.2. Calculations. Born-Oppenheimer Molecular Dynamics (BOMD) calculations were performed as described previously. ^{14,15} Briefly, multiple trajectories were run with the valence-electron PM6-D3H4 calculations 16 for 20 ps with 1 fs steps using the Berendsen thermostat 17 at 410-610 K and under

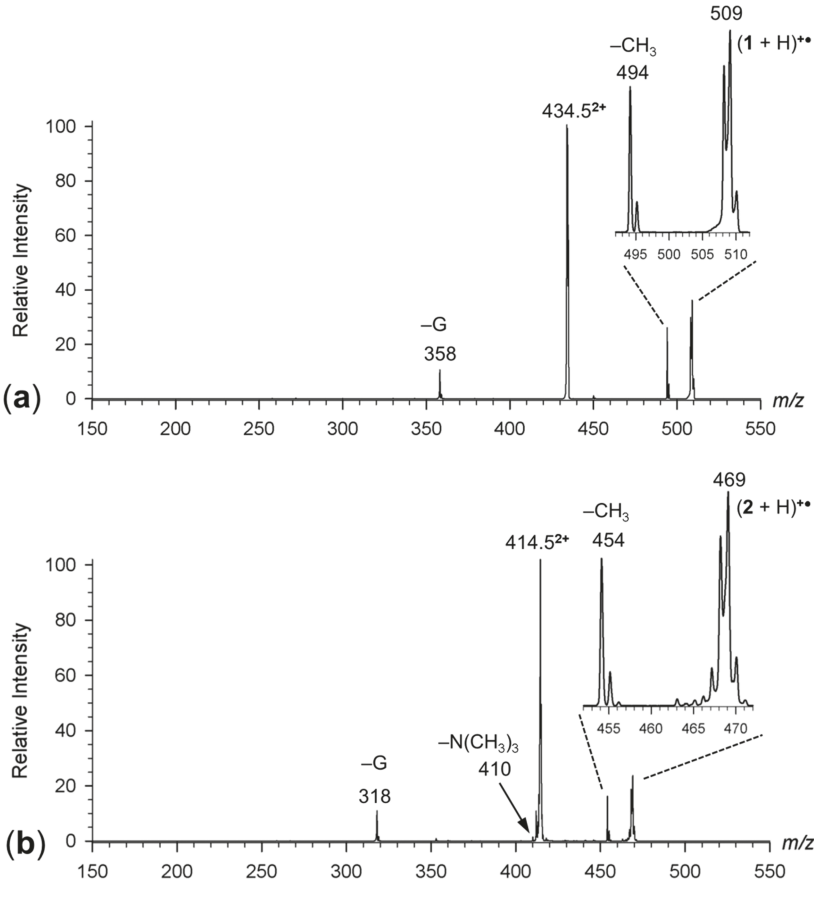


Figure 1. ETD spectra of complexes (a) $(1 + DBCE + H)^{2+}$ at m/z 434.5 and (b) $(2 + DBCE + H)^{2+}$ at m/z 414.5.

the Cuby4 platform. 18 The PM6-D3H4 calculations were run with MOPAC 16.19 Two hundred snapshots were extracted at regular intervals from 20000 steps in each trajectory, reoptimized with PM6-D3H4, and the list of structures was compacted by sorting out duplicates. Selected low-energy conformers were reoptimized with $B3LYP/6-31+G(d,p)^{20}$ to provide harmonic frequencies. These were used to calculate enthalpies and entropies at 310 K corresponding to the experimental temperature. Hindered rotors were identified by the procedure included in Gaussian 16^{21,22} and used to correct the calculated entropies. Another set of optimized structures were obtained by M06-2X/ $6-31+G(d,p)^{23}$ geometry optimizations, followed by M06-2X/6-311++G(2d,p) calculations of single-point energies. Transition states were located by a stepwise procedure. First, the potential energy surface along the reaction coordinate was mapped by a stepwise bond lengthening in low-energy reactant conformers, and the TS was gradient-optimized to the first-order saddle point with one imaginary frequency. Several thus-obtained transition states were then treated by BOMD at 610 K using the Cuby4 platform in which the bond lengths in the reaction center were fixed at their original TS values while the other internal coordinates were dynamically free. Snapshots from these runs were sorted out by DFT while keeping the TS coordinates fixed, and the resulting conformers were sorted out by energy. Finally, a search was performed for low-energy geometries to arrive at the final, conformationally optimized, TS structures which were confirmed by harmonic frequency analysis. Isotopologue frequencies were calculated using the B3LYP harmonic force constants. Excited-state calculations were performed with timedependent DFT²⁴ (TD-DFT) with M06-2X/6-31+G(d,p) for

50 excited states. The choice of this functional and basis set for TD-DFT was based on our previous benchmarking 25,26 against equation-of-motion coupled cluster calculations 27 for other nucleobase radicals. Vibronic transitions were calculated for 12–24 excited states from Wigner configurations 28,29 that were generated from 198 harmonic vibrational modes of $(2 + H)^{+\bullet}$ using the Newton X 16 program. 30 Typically, 300 lowest energy configurations were selected by their Boltzmann factors for TD-DFT calculations.

3. RESULTS AND DISCUSSION

3.1. Cation-Radical Formation, Characterization, and **Dissociation Kinetics.** Electrospray ionization of 1^+ and 2^+ yielded doubly charged ions, $(1 + H)^{2+}$ and $(2 + H)^{2+}$, respectively, that were characterized by accurate mass measurements and collision-induced dissociation (CID) spectra (Figure S1a,c). The CID spectrum of $(2 + H)^{2+}$ (m/z 234.6) was very simple, displaying the complementary (G + H)+ and $C_{15}H_{29}N_2O_5^+$ fragment ions formed by cleavage of the glycosidic C-1'-N-9 bond (Figure S1c). The CID spectrum of $(1 + H)^{2+}$ (m/z 254.5) displayed additional fragment ions from the dioxolan ring cleavage (m/z 299, Figure S1a). The CID spectrum of 1^+ (m/z 508) was also measured for reference (Figure S1b). However, electron transfer to $(1 + H)^{2+}$ and $(2 + H)^{2+}$ H)²⁺ resulted in a complete dissociation, forming the 1⁺ and 2⁺ ions and fragments by loss of NMe₃, while the desired $(1 + H)^{+\bullet}$ and $(2 + H)^{+\bullet}$ cation radicals were absent (Figure S2a,b). This result was not completely unexpected, in view of the substantial exoergicity of electron transfer to the dications and the fragility of nucleoside radicals. 31,32 To facilitate the formation of stable (1 +

H)^{+•} and (2 + H)^{+•} we generated by electrospray ionization doubly charged noncovalent complexes of $(1 + H)^{2+}$ and (2 + H)²⁺ with 2,3:11,12-dibenzo-18-crown-6-ether (DBCE) (m/z 414.5 and 434.5, respectively) and used these for ion—ion electron-transfer reactions with the fluoranthene anion.¹⁰ The resulting spectra indicated the formation of stable cation-radicals at m/z 509 and 469 for $(1 + H)^{+•}$ and $(2 + H)^{+•}$, respectively (Figure 1a,b). We also generated the $(D_4-1+D)^{+•}$ and $(D_6-2+D)^{+•}$ radicals in which all the exchangeable N—H and O—H were replaced by deuterium (m/z 514 and 476, Figure S3a,b). The ETD spectra of the DBCE complexes still showed that, regardless of the protecting groups on ribose, the guanosine cation radicals underwent substantial dissociation. The main dissociations were loss of H, CH₃, and guanine, as annotated in the Figure 1a,b and Figure S3a,b spectra.

The loss of H or D was the most facile dissociation that occurred even upon storing the cation radicals in the ion trap without any activation. In addition, a spontaneous loss of guanine was also observed as a minor dissociation. The peaks of the mass-selected $(1 + H)^{+\bullet}$, $(D_4-1+D)^{+\bullet}$, $(2 + H)^{+\bullet}$, and $(D_6-1+D)^{+\bullet}$ ions showed tails on the low m/z sides that were indicative of metastable species that dissociated prior to resonant ejection from the ion trap (Figure 2a,b). 33-35 These tails were particularly prominent at short storage times and gradually diminished as the ions were kept longer in the ion trap (Figure S4a,b). We utilized these spontaneous dissociations of massselected ions at m/z 509, m/z 514, m/z 469, and m/z 476 for (1 + H) $^{+\bullet}$, $(D_4-1+D)^{+\bullet}$, $(2+H)^{+\bullet}$, and $(D_6-2+D)^{+\bullet}$, respectively, to monitor the reaction kinetics and determine the apparent unimolecular dissociation rate constants. The logarithmic plot for the $(D_4-1+D)^{+\bullet}$ relative intensity was linear, giving the rate constant, $k_D(1) = 0.58 \text{ s}^{-1} (r^2 = 0.999)$ (Figure 2c), for the overall dissociation which was composed of the rate constants for the competitive loss of D, $k_D(D\text{-loss})(1) = 0.54 \text{ s}^{-1}$ and loss of guanine, $k_D(G-loss)(1) = 0.03 \pm 0.006 \text{ s}^{-1}$. The plot for $(1 + 1)^{-1}$ H)^{+•} was less tight ($r^2 = 0.978$), giving the overall rate constant $k_{\rm H}(1) = 0.28 \, {\rm s}^{-1}$ that was composed of $k_{\rm H}({\rm H\text{-}loss})(1) = 0.26 \, {\rm s}^{-1}$ and $k_{\rm H}(\text{G-loss})(1) = 0.02 \pm 0.005 \,\text{s}^{-1}$. Thus, the loss of hydrogen exhibited an inverse isotope effect of $k_{\rm H}({\rm H\text{-}loss})(1)/k_{\rm D}({\rm D\text{-}}$ loss)(1) = 0.48.

The kinetic plot for the $(2 + H)^{+\bullet}$ relative intensity $(\ln x(H))$, Figure S4c) showed a linear part after ca. 400 ms that was leastsquares fitted giving the combined rate constant for both dissociation channels as $k_H(2) = k_H(H-loss)(2) + k_H(G-loss)(2)$ = 0.28 s^{-1} with the correlation coefficient of r^2 = 0.99. From the combined rate constant and the product ion intensity ratios we obtained $k_{\rm H}({\rm H\text{-}loss})(2)$ and $k_{\rm H}({\rm G\text{-}loss})(2)$ as 0.26 and 0.02 \pm 0.005 s⁻¹, respectively. At earlier ion residence times, the plot showed a steeper descent with an apparent $k_{\rm H}(2) = 0.62$ and a poorer fit $r^2 = 0.95$. The plot for $(D_6-2+D)^{+\bullet}(x(D), Figure S4c)$ showed an overall linear function with $k_D(2) = k_D(D-loss)(2) +$ $k_{\rm D}(\text{G-loss})(2) = 0.45 \text{ s}^{-1}$ and $r^2 = 0.99$, although the first few points up to 100 ms also indicated a faster dissociation. The faster-dissociating $(2 + H)^{+\bullet}$ and $(D_6-2 + D)^{+\bullet}$ ions were likely to belong to fractions that were nonresonantly excited upon ion isolation and underwent CID. In contrast, the longer-lived ions were likely to be thermalized to undergo spontaneous dissociations. From the $k_D(2)$ we obtained the rate constants $k_{\rm D}({\rm D\text{-}loss})(2)$ and $k_{\rm D}({\rm G\text{-}loss})(2)$ as 0.39 and 0.06 \pm 0.02 s⁻¹, respectively. The kinetic data indicated that the dissociation of the long-lived ions $(2 + H)^{+\bullet}$ also displayed an inverse isotope effect of $k_{\rm H}({\rm H\text{-}loss}(2)/k_{\rm D}({\rm D\text{-}loss})(2) = 0.65$ that was of a similar magnitude as that measured for $(1 + H)^{+\bullet}$.

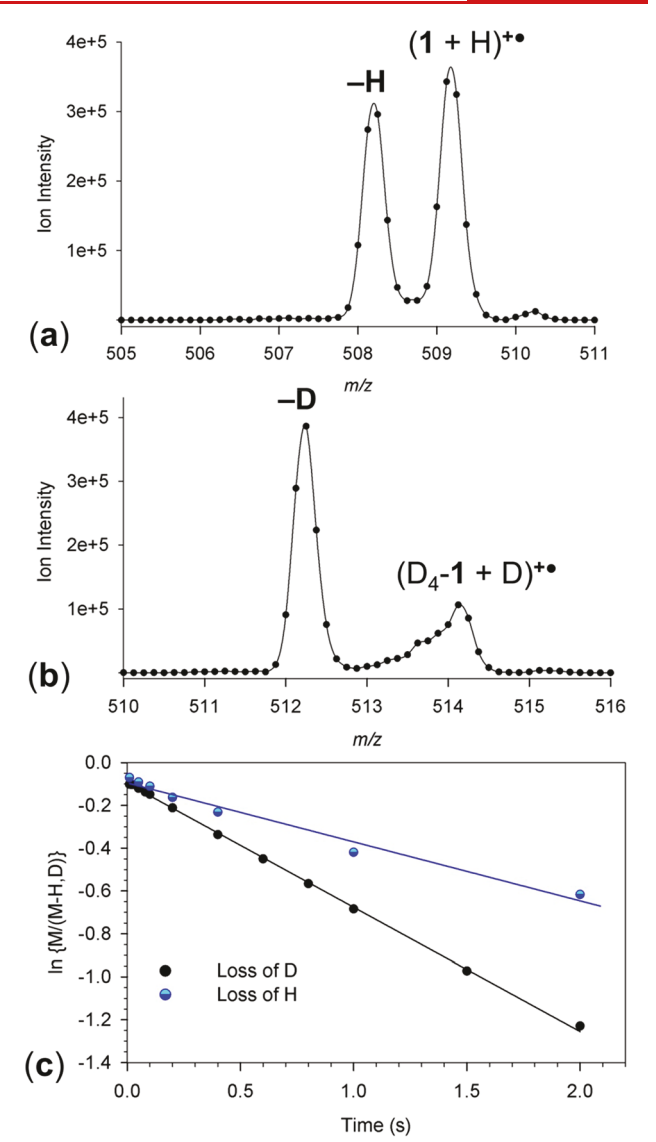


Figure 2. Peak profiles for (a) $(1+H)^{+\bullet}$ and (b) $(D_4\text{-}1+D)^{+\bullet}$ ions that were isolated by mass and stored without excitation in the ion trap for 2 s. (c) Logarithmic kinetic plots of precursor ion relative intensities for $(1+H)^{+\bullet}$ and $(D_4\text{-}1+D)^{+\bullet}$, respectively, with lines of least-squares fits.

The $(1 + H)^{+\bullet}$ and $(2 + H)^{+\bullet}$ ions, as well as their deuterated analogues, were further investigated by CID-MS³. Upon lowenergy excitation, the $(2 + H)^{+\bullet}$ ion chiefly lost an H atom and guanine (m/z 318). Note that the m/z 468 peak due to loss of H was in part obscured by the metastable tail of the m/z 469 precursor (Figure 3a). At higher excitation amplitudes, $(2 + H)^{+\bullet}$ underwent further dissociations by a combined elimination of guanine and $C_2H_3O_2$ from the ribose ring (m/z 259), and a carbamate elimination forming the m/z 203 fragment ion (Figure 3b). CID-MS³ at high excitation amplitudes of $(D_6-2 +$ D)+• displayed an equal loss of H and D (Figure 3c), which contrasted with the spontaneous dissociation leading to a predominant loss of D (Figure 2b). The clean elimination of D_{4^-} G (m/z 321) from $(D_6-2+D)^{+\bullet}$, as well as the isotope mass shifts in the other fragment ions $(m/z 259 \rightarrow m/z 261)$, and $m/z 203 \rightarrow$ m/z 205), clearly indicated that there was no exchange between the guanine deuterium atoms and hydrogen atoms in other parts of the ion.

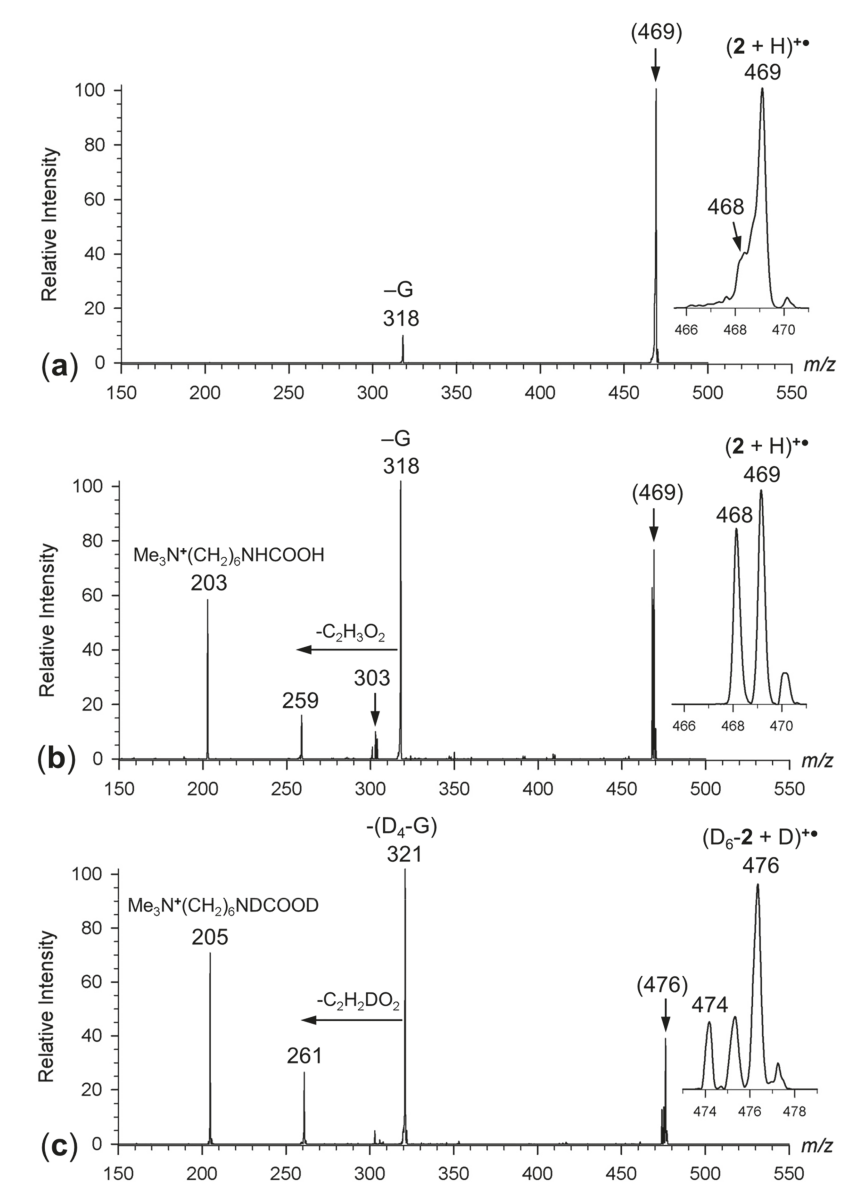


Figure 3. CID-MS³ spectra of (a) $(2 + H)^{+\bullet}$ at a low excitation amplitude; (b) $(2 + H)^{+\bullet}$ at a high excitation amplitude; (c) $(D_6-2 + D)^{+\bullet}$ at a high excitation amplitude. Insets show the precursor ion and H/D-loss peak profiles.

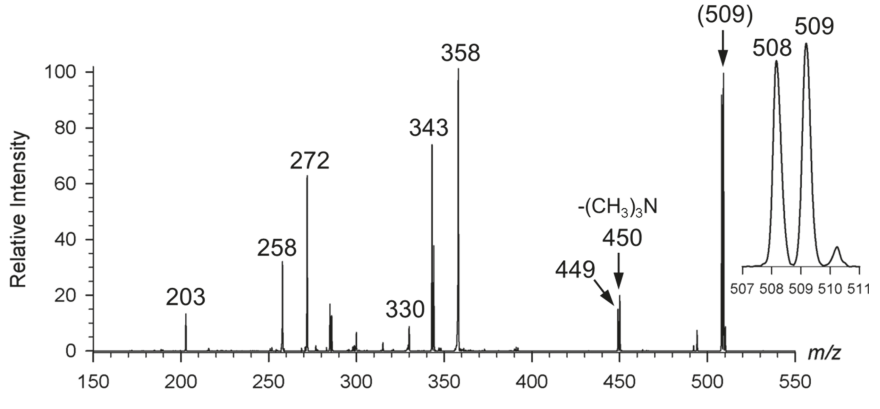


Figure 4. CID-MS³ spectrum of $(1 + H)^{+\bullet}$. Inset shows the precursor ion and H-loss peak profiles.

The CID spectrum of $(1 + H)^{+\bullet}$ (Figure 4) showed additional fragment ions besides those by loss of H (m/z 508) and guanine (m/z 358). Loss of trimethylamine (m/z 450) in combination with loss of H (m/z 449) was substantially more abundant than

for $(2 + H)^{+\bullet}$. The CID spectrum of $(1 + H)^{+\bullet}$ newly displayed fragment ions at m/z 344, 343, and 272. The m/z 344 and 343 ions were formed by elimination of $C_6H_7N_5O$, the latter following a hydrogen atom loss. Note that the m/z 343 fragment

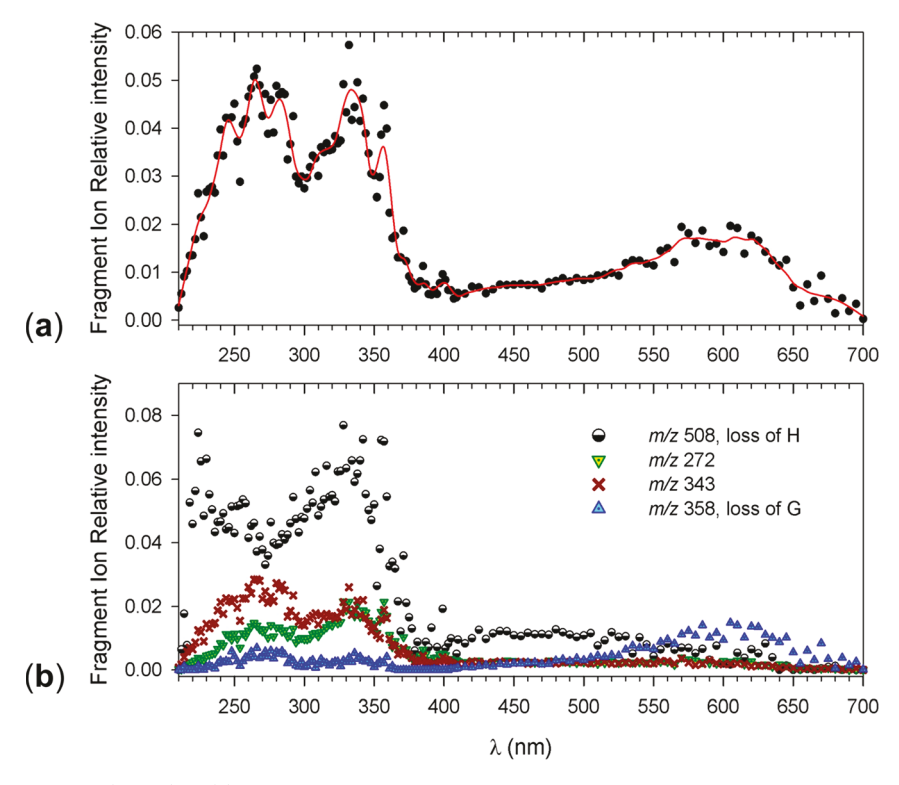


Figure 5. UV—vis action spectra of $(1 + H)^{+\bullet}$. (a) Sum of photofragment ion relative intensities not including the m/z 508 (loss of H) channel. (b) Individual photofragment channels.

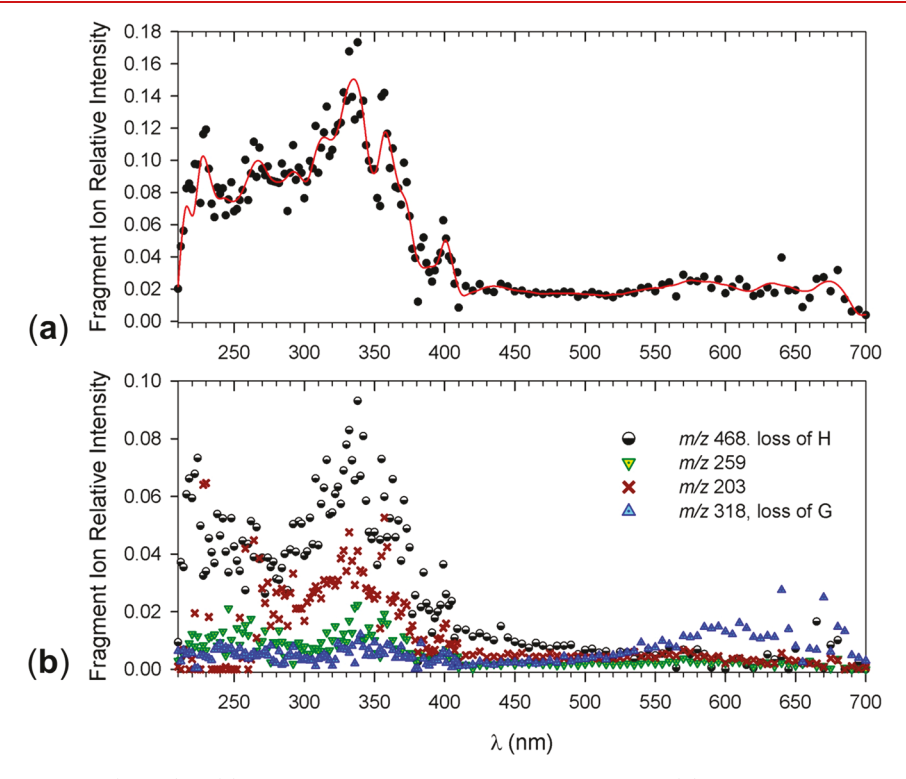


Figure 6. UV-vis action spectra of (2 + H)⁺•. (a) Sum of photofragment ion relative intensities. (b) Individual photofragment channels.

ion is prominent in the CID spectrum of 1^+ (Figure S1b), indicating a methyl transfer to the guanine ring. A similar dissociation was seen in the UVPD spectrum of 2^+ (m/z 303, Figure S5b) and also for adenosine conjugate cation radicals, as has been reported recently.³² This reaction is facilitated by an interaction of the trimethylammonium group in the conjugate

with the guanine ring which functions as a nucleophile in singly charged ions. Note that methyl transfer is absent in CID of doubly charged ions (Figure S1a,c) where the charged trimethylammonium and protonated guanine ring are kept apart by Coulomb repulsion. The m/z 272 and 258 ions are

probably formed by cleavages within the ribose ring following the loss of guanine and methylguanine.

3.2. Action Spectra. The fragment ions identified by CID- MS^3 were selected for monitoring the photodissociation of (1 +H)^{+•} and $(2 + H)^{+•}$. The action spectrum of $(1 + H)^{+•}$ was composed of the abundant m/z 508, 358, 343, and 272 photofragment ions. The combined m/z 358, 343, and 272 photofragment ion intensities are plotted in Figure 5a. This showed composite bands with maxima at 260 and 330 nm and a broad band at 600 nm. The loss of guanine (m/z 358) channel was the main contributor to the 600 nm band, whereas the 260 and 330 nm bands had contributions from all major channels (Figure 5b). The m/z 508 channel (loss of H) displayed another band at 210 nm and a broad featureless band between 400 and 580 nm. However, the m/z 508 peak was partly obscured by the low-mass shoulder of the m/z 509 precursor because of its metastable dissociation that was most pronounced in regions of low photodissociation conversion. This made the intensity measurements at m/z 508 difficult, and it may have affected the action spectrum based on this ion channel.

The action spectrum of $(2 + H)^{+\bullet}$ was monitored at m/z 468, 318, 259, and 203. The combined spectrum is shown in Figure 6a, and the individual fragment ion channels are plotted in Figure 6b. The action spectrum displayed absorption bands at 270 and 330 nm and a broad band at 580 nm. Similar to $(1 + H)^{+\bullet}$, the 580 nm band was mainly due to the m/z 318, loss of guanine, channel which likely represented a low-energy dissociation, dominating at low photon energies. The 330 nm band was split in the m/z 318, 259, and 203 channels that showed small wavelength shifts from 330 nm for the m/z 203 channel to 340 and 350 nm for the m/z 318 and m/z 259 channels, respectively. These shifts were probably caused by energy-dependent competitive kinetics of these dissociations, whereby the lowenergy m/z 318 channel showed the longest wavelength band onset and maximum. The intensity of the m/z 468 (loss of H) ion was again affected by an overlap with the metastable shoulder of the m/z 469 precursor ion, especially in wavelength regions of low absorbance. We attempted to mitigate this interference by fitting the m/z 469 and m/z 468 with Gaussian profiles and integrating those while ignoring the metastable tail. Nevertheless, this procedure was imperfect, and the remaining interference may explain the featureless bands at 400-500 nm and above 600 nm in the m/z 468 channel (Figure 6b).

The action spectrum of $(2 + H)^{+\bullet}$ is to be matched against the action spectra of the closed-shell dication $(2 + H)^{2+}$ having a protonated guanine ring (Figure S5a) and cation 2+ with a neutral guanine moiety (Figure S5b). The spectrum of $(2 + H)^{2+}$ displayed three bands with maxima at 245, 260, and 285 nm that were traced by both major photofragment ions which were (G+ H)⁺ at m/z 152 and its complementary ion formed by loss of guanine (m/z 317). The spectrum of 2^+ also showed three bands with a major absorption at 240 nm that was carried by the rearrangement ion at m/z 303. The other bands at 265 and 280 nm had contributions also from the other photofragment ions at m/z 152 and m/z 317. The spectrum of $(2 + H)^{2+}$ indicated a 10 nm red shift for all three bands compared to the spectrum of 2⁺ that can be attributed to the guanine ring protonation. Note that the guanine π -electron system is the only chromophore absorbing in this wavelength region. More significantly, the spectra of the closed-shell ions did not display any absorption above ca. 300 nm. Thus, the characteristic bands in the action spectrum of $(2 + H)^{+\bullet}$ (340 and 580 nm) can be unequivocally assigned to electron excitations in the guanine radical.

3.3. Ion Structures and Action Spectra Assignment. We carried out extensive calculations of cation—radical structures pertinent to $(1 + H)^{+\bullet}$ and $(2 + H)^{+\bullet}$, as well as their ion precursors, dissociation products, and transition states leading to major dissociations. The primary goal of these calculations was to assign the action spectra, with a secondary goal of establishing the relative energies of guanine ion and radical protomers and their conformers. Starting with $(1 + H)^{+\bullet}$, we used Born—Oppenheimer Molecular Dynamics (BOMD) calculations to map the conformational space of guanine, ribose, and the carbamate side chain and then applied DFT for full gradient optimization of low-energy structures identified by BOMD. The relative energies of $(1 + H)^{+\bullet}$ protomers with hydrogen attachment sites at guanine positions N-3, O-6, N-7, and NH₂ (N-10) are summarized in Table 1. The DFT calculations

Table 1. Relative Energies of Cation Radicals (1 + H)+•

	relative energy ^{a,b}	
ion	$M06-2X/^{c} 6-31+G(d,p)$	$M06-2X/^{c,d}$ 6-311++G(2d,p)
1a ^{+•}	0 (0)	0 (0)
1b ^{+•}	9.5 (5.7)	9.0 (5.2)
1c+•	3.1 (0.2)	4.9 (2.0)
1d⁺•	6.4 (2.7)	6.6 (2.9)
1e ^{+•}	12 (8.1)	14 (10)
1f ^{+•}	24 (22)	24 (23)
1g ^{+•}	56 (62)	61 (67)

^aIn kJ mol⁻¹; ^bIncluding scaled B3LYP/6-31+G(d,p) zero-point energies and referring to 0 K unless stated otherwise. ^cRelative free energies at 310 K in parentheses. ^dSingle-point energies on M06-2X/6-31+G(d,p) optimized geometries.

indicated very close relative free energies of protomers protonated at N-7 ($1a^{+\bullet}$ and $1b^{+\bullet}$), N-3 ($1c^{+\bullet}$ and $1d^{+\bullet}$), and O-6 ($1e^{+\bullet}$) (Figure 7) where the differences were within the usual accuracy limits of the DFT methods employed. Thus, no preference for either structure could be inferred from the energy calculations. The low-energy (1 + H)^{+•} ions displayed some interesting structural features that are briefly discussed here. In contrast to the cation radicals, energy analysis of the (1 + H)²⁺ dications gave N-7-protonated tautomers as the lowest free-energy structures (Figure S6). This result was consistent with the preferred protonation at N-7 in gas-phase guanine^{36,37} and guanosine.³⁸

The low-energy N-7-H cation-radical tautomers (1a++ and 1b+•) were pyramidized at C-8, displaying a high atomic spin density at this position (Figure 7). The charge-carrying side chain was folded toward the guanine ring such that the proximate trimethylammonium hydrogens were within 2.7 Å of the radical carrying C-8. The N-3-H tautomers $(1c^{+\bullet})$ and $1d^{+\bullet}$ showed a high spin density at C-2 which was pyramidized. The side chain in these tautomers was folded to become sandwiched with the guanine ring, but the closest approach of the trimethylammonium hydrogens was toward O-6, not the C-2 radical center. The O-2-H tautomers ($1e^{+\bullet}$ and $1f^{+\bullet}$) carried most of the spin density at C-6. The side chain was folded with the proximate trimethylammonium hydrogens approaching N-7 within 2.4 Å. Finally, the less stable ion 1g^{+•} had a substantial spin density at C-2, and the side chain was tightly folded toward the guanine ring with O6···H distances within 2.3 Å. The side chain folding was chiefly due to charge-dipole interactions between the trimethylammonium group and the ring N or O atoms of high electron density. Hydrogen bonding involving the carbamate

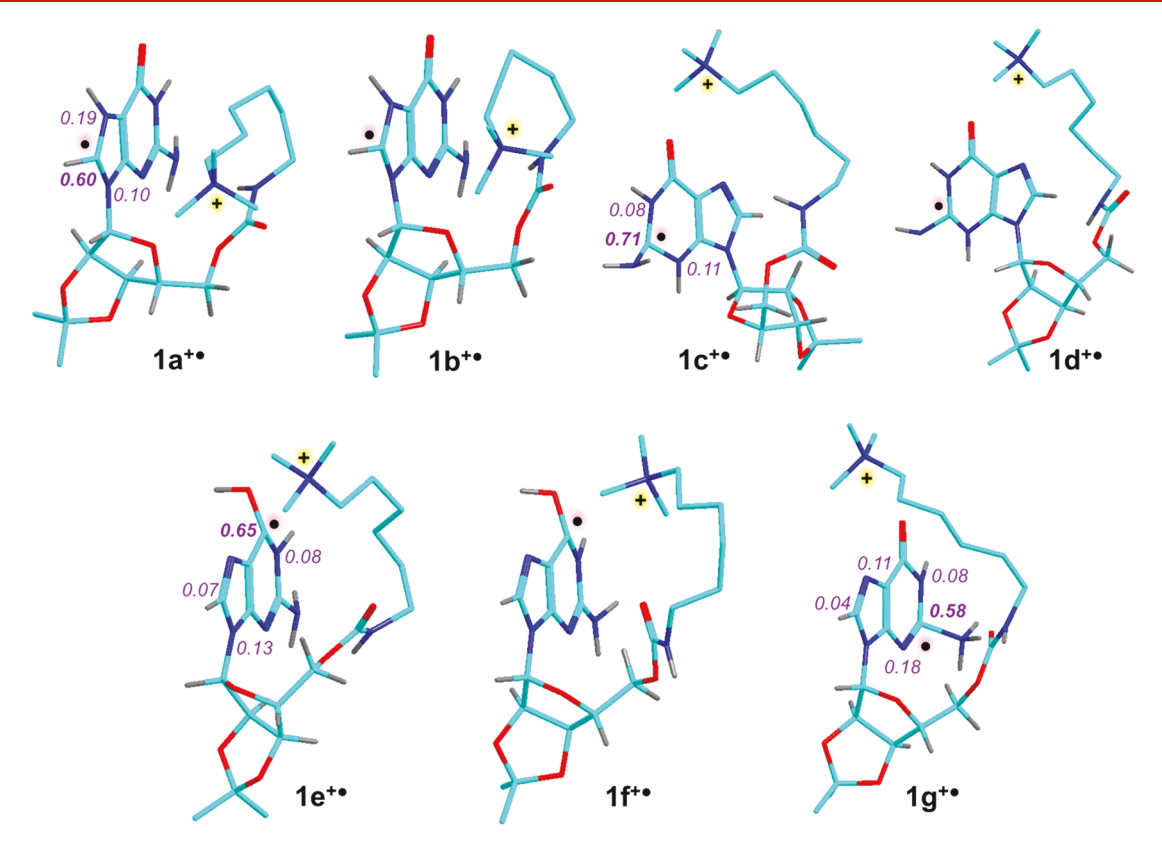


Figure 7. M06-2X optimized structures of low-energy $(1 + H)^{+\bullet}$ isomers. Atom color coding is as follows: cyan = C, blue = N, red = O, gray = H. The side-chain aliphatic hydrogens were hidden to avoid clutter. Major atomic spin densities are shown as purple italics.

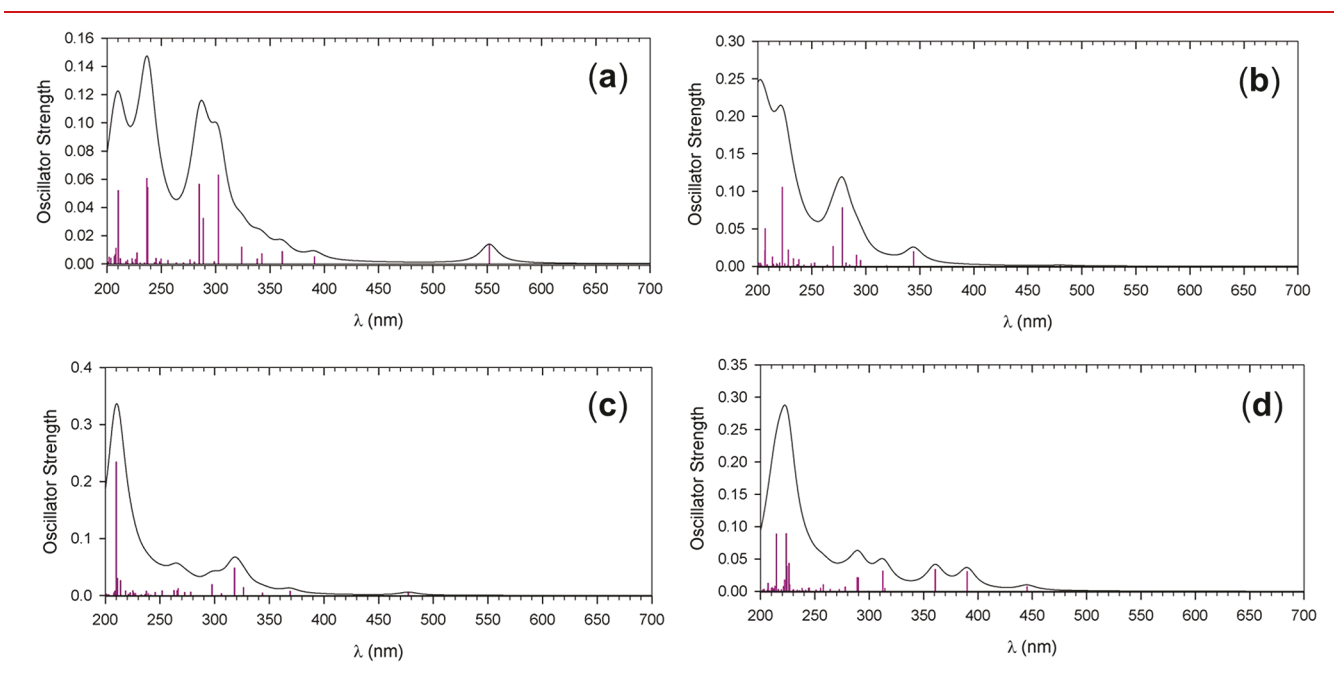


Figure 8. M06-2X/6-31+G(d,p) TD-DFT absorption spectra of (a) $1a^{+\bullet}$, (b) $1c^{+\bullet}$, (c) $1e^{+\bullet}$, and (d) $1g^{+\bullet}$. The band profiles are from artificial broadening of the transition lines by convolution with Lorentzian functions at 10 nm full width at half-maximum (fwhm).

linker was less important, as judged from the CO-N-H \cdots ring N distances which were 2.41, 2.90, and 2.76 Å in $1a^{+\bullet}$, $1c^{+\bullet}$, and $1e^{+\bullet}$, respectively. Ion $1g^{+\bullet}$ was different as it developed a strong hydrogen bond between the NH $_3$ group and the carbamate carbonyl at 1.75 Å.

We used TD-DFT to calculate electronic excitations in $1a^{+\bullet}$ – $1g^{+\bullet}$ that were plotted in Figure 8 for the lowest energy

conformers. The others are shown in Figure S7. Comparison of the calculated spectra with the action spectrum of $(1 + H)^{+\bullet}$ revealed a match of the long-wavelength band $(\lambda_{max} = 550 \text{ nm})$ of $1a^{+\bullet}$ (Figure 8a) with the band of $(1 + H)^{+\bullet}$ in same region (Figure 5a). Similarly, the calculated bands of $1a^{+\bullet}$ at 240 and 290 nm found a match with the action spectrum bands at 260 and 340 nm, considering a vibronic red shift and band broadening. A

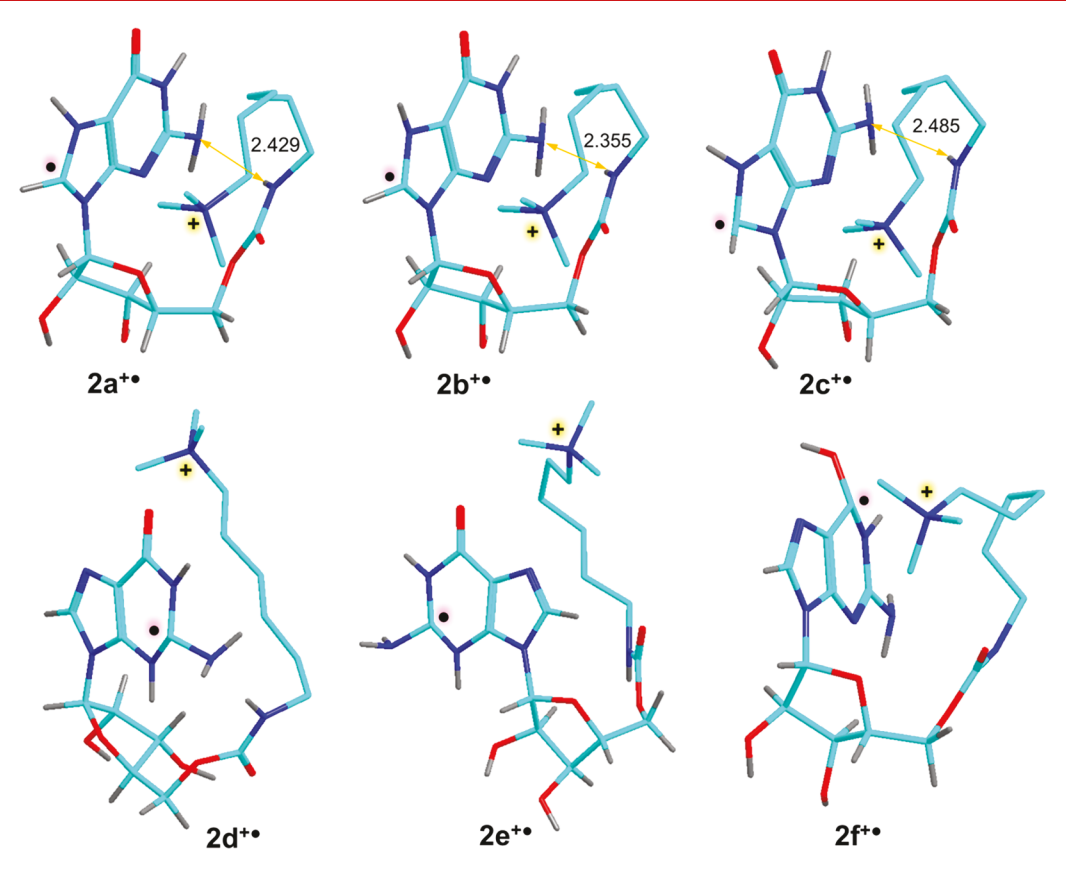


Figure 9. M06-2X-optimized structures of low-energy $(2 + H)^{+\bullet}$ isomers. Atom color coding is as follows: cyan = C, blue = N, red = O, gray = H. The side-chain aliphatic hydrogens were hidden to avoid clutter.

similar match was observed for the other N-7-protonated lowenergy conformer $1b^{+\bullet}$ (Figure S7a). In contrast, the other guanine protomers, $1c^{+\bullet}$, $1e^{+\bullet}$, and $1g^{+\bullet}$ and their conformers displayed various degrees of mismatch with the action spectrum in the characteristic 500-600 and 300-400 nm regions (Figure 8b-d). Thus, the action spectrum of $(1+H)^{+\bullet}$ pointed to the N-7 protonated tautomer $1a^{+\bullet}$ or its low-energy conformer $1b^{+\bullet}$.

We further addressed the structures, energies, and absorption spectra of isomers pertaining to $(2 + H)^{+\bullet}$. The optimized geometries of the lowest energy conformations of tautomers $2a^{+\bullet}-2f^{+\bullet}$, originating from ions protonated at the basic N-1, N-3, N-7, and O-6 sites, are shown in Figure 9, for relative energies see Table 2. The N-7-protonated isomers $2a^{+\bullet}$ and $2b^{+\bullet}$ were the lowest free energy ions that differed in the exo and endo configuration at the pyramidal N-7 atom. These two forms were calculated to be freely convertible by inversion at N-7. The transition-state energy for the inversion, when corrected for zero-point vibrational energy, was below those of 2a+• and 2b+•. Another isomer $(2c^{+\bullet})$, having an inverted configuration at C-8, was slightly higher in energy. In addition to $2a^{+\bullet}-2c^{+\bullet}$, we found the N-3-H tautomer $(2d^{+\bullet})$ and the O-6-enol form $(2f^{+\bullet})$ to be within 10 kJ mol⁻¹ of 2a^{+•}. Thus, according to the optimized structures and energies, there was no particular preference for either guanosine radical tautomer. It may be noted that the ordering of free energies for $2a^{+\bullet}-2f^{+\bullet}$ was affected by the ion entropies. Because of the side-chain flexibility, the low frequency modes were treated as hindered rotors according to McClurg et al.,²² resulting in upward entropy corrections.

The optimized structures of $2a^{+\bullet}-2f^{+\bullet}$ displayed close similarities with those of $1a^{+\bullet}-1g^{+\bullet}$, as far as the interactions between the charged side chain and the radical-carrying guanine

Table 2. Relative Energies of Cation Radicals $(2 + H)^+$

	relative energy ^{a,b}	
ion	$M06-2X/^{c} 6-31+G(d,p)$	$M06-2X/^{c,d}$ 6-311++G(2d,p)
2a ^{+•}	0 (0)	0 (0)
2b ^{+•}	3 (-3.4)	4.2 (-2.1)
2c ^{+•}	5.9 (7.8)	6.3 (8.2)
2d ^{+•}	-8.6 (1.4)	-3.7 (6.4)
2e ^{+•}	6.2 (11)	9.3 (14)
2f ^{+•}	7.9 (4.0)	8.3 (4.3)
$2g^{+\bullet}$	-66 (-65)	-65 (-64)
2h ^{+•}	-14 (-15)	-14 (-14)
2i ^{+•}	8.0 (7.0)	8.1 (7.2)
2j ^{+•}	57 (56)	59 (59)
2k ^{+•}	74 (66)	75 (67)
2l ^{+•}	-11 (0.6)	-13 (-1.6)
3+ + H•	62 (35)	59 (32)
4 ^{+•} + Guanine	52 (-6.9)	46 (-13)
TS1	92	94
D ₇ -TS1	103 ^e	105 ^e
TS2	92	104
TS3	106	106
TS4	101	104
D ₇ -TS4	107^{e}	110 ^e
TS5	. 95	97

"In kJ mol⁻¹; "Including scaled B3LYP/6-31+G(d,p) zero-point energies and referring to 0 K unless stated otherwise. "Relative free energies at 310 K in parentheses. "Single-point energies on M06-2X/6-31+G(d,p) optimized geometries. "Relative to D_7 -2a^{+•}.

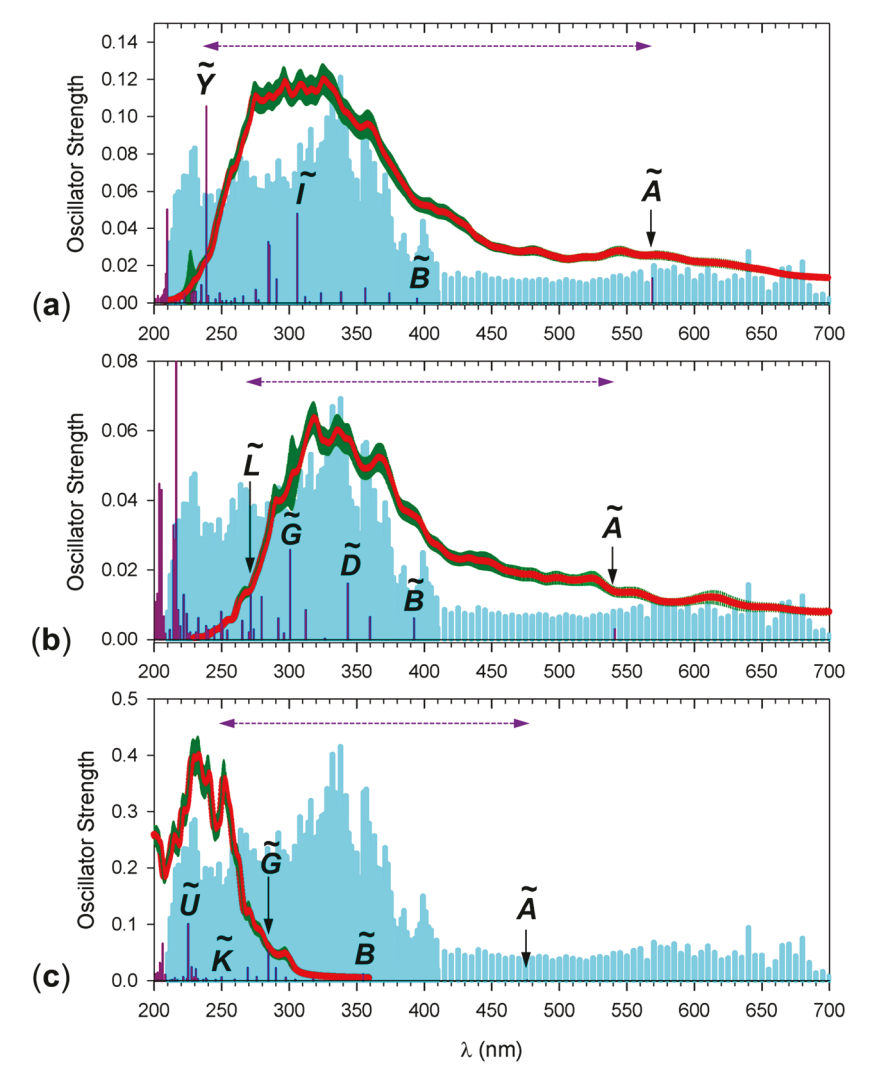


Figure 10. M06-2X/6-31+G(d,p) calculated vibronic absorption spectra of (a) $2a^{+\bullet}$, (b) $2f^{+\bullet}$, and (c) $2d^{+\bullet}$ tautomers of $(2 + H)^{+\bullet}$. The scaled action spectrum is shown as cyan background. The double arrows indicate the range of excited-state wavelengths used in the vibronic calculations.

ring were concerned. For example, the N-7-H tautomers $2a^{+\bullet}-2c^{+\bullet}$ showed folded conformations in which the trimethylammonium group was in the vicinity of the radical-carrying imidazole ring, a situation also encountered with $1a^{+\bullet}$ and $1b^{+\bullet}$. The absence of the rigid 1,3-dioxolan ring in $2a^{+\bullet}-2f^{+\bullet}$ affected the ribose ring conformation. For example, the O-2–C-2'–C-3'–O-3 dihedral angle in $2a^{+\bullet}$ (31.0°) was larger than in $1a^{+\bullet}$ (-3.5°). However, the side-chain conformation allowing the ion-dipole interactions was established to a similar manner in $2a^{+\bullet}$ and $1a^{+\bullet}$, as set up by the similar O-5–C-5'–C-4'–C-3' dihedral angles (54.7° and 43.7°, respectively). Thus, the presence of the dioxolan ring in $1a^{+\bullet}-1g^{+\bullet}$ had only a minor effect on the ion conformations and tautomer relative free energies.

For the optimized structures of $2a^{+\bullet}$, $2d^{+\bullet}$, and $2f^{+\bullet}$ we calculated TD-DFT electronic excitations that were expanded to 300 configurations at 310 K to provide vibronic spectra. Because of the size of these ions and the large number of low-oscillator strength excited states in open-shell systems, we limited the number of excited states included in the vibronic calculations to 12-24 states to cover the wavelength range in the visible and near-UV regions. The calculated vibronic spectra along with the excited state assignments are shown in Figure 10. The spectrum of $2a^{+\bullet}$ (Figure 10a) displayed a broad band at 569 nm due to an

excitation to the first (A) excited state. This calculated band, including its vibronic broadening, was in a close agreement with the 580 nm band in the action spectrum (Figure 6a). The transition to the A state was identified as a dipole-allowed $\pi_z \rightarrow$ π_z^* excitation from the singly occupied molecular orbital (SOMO, MO126) to the virtual orbital space (Figure S8). The next three transitions for 2a^{+•} (B, C, and D excited states at 395, 374, and 357 nm, respectively), with the pertinent vibronic broadening, gave rise to the broad composite band at 350-450 nm. These excitations occurred from the SOMO to molecular orbitals of the Rydberg (B state) and mixed π_z^* -Rydberg (C and D states) type (Figure S8). The intense transition to the I state (306 nm) was due to a $\pi_z \to \pi_z^*$ type excitation from the doubly occupied MO125, occurring within the α -MO manifold. Finally, another intense transition to the Y state (239 nm) was also of the $\pi_z \to \pi_z^*$ type occurring from the doubly occupied MO125, but within the β -MO manifold. In contrast, the absorption spectrum of the N-3-H tautomer (2d+*) displayed only very weak transitions in the visible and near-UV regions, as exemplified by the A and B states at 476 and 355 nm (Figure 10c). The major bands at 225-230 nm in the calculated vibronic spectrum of $2d^{+\bullet}$ were not prominently represented in the action spectrum. These combined features eliminated 2d^{+•} as a plausible structure candidate. The absorption spectrum of the O-6-H tautomer

Scheme 2. M06-2X/6-31+G(d,p)-Optimized Transition States, Intermediate Complexes, and Dissociation Products^a

^aRelative 0 K energies in kJ mol⁻¹ in parentheses.

 $(2f^{\bullet \bullet})$ did show some similarities with the action spectrum due to excitation to the B-L states in the 270–400 nm region (Figure 10b). However, the band pertaining to the transition to the A state (541 nm) was spread over a broad range of wavelengths upon vibronic broadening and did not represent a recognizable feature. Similarly, the most intense transition in $2f^{\bullet \bullet}$ at 216 nm (Figure 10b) was not realized as an intense band in the action spectrum. On the basis of this comparison, and considering the match of the closely related $1a^{\bullet \bullet}$ absorption spectrum with the action spectrum of $(1+H)^{\bullet \bullet}$ (Figure 8a), we conclude that both these gas-phase ions were N-7-H tautomers.

3.4. Ion Dissociations and Isotope Effects. The spontaneous loss of H and guanine from thermal (1 + H)+• and $(2 + H)^{+\bullet}$ suggested that these dissociations had low activation energies, similar to those previously reported for adenosine conjugates.³² The spontaneous loss of H chiefly (>95%) involved the exchangeable hydrogens in $(1 + H)^{+\bullet}$ and (2 + H)+•, as evidenced by the spectra of the D-labeled analogues. Upon collisional activation of $(D_6-2+D)^{+\bullet}$, there was a 50/50 loss of H and D from the guanine moiety (Figure 3c, inset). Loss of H can proceed in $1a^{+\bullet}-1g^{+\bullet}$ and $2a^{+\bullet}-2f^{+\bullet}$ to convergently form the lowest energy guanine N-1-H tautomer, such as 3+ (Scheme 2). We used BOMD and DFT calculations to determine the transition states (TS) for the dissociation of the N-7-H bond in $2a^{+\bullet}$ and $2b^{+\bullet}$. The loss of H from $2a^{+\bullet}$ had a low threshold energy of $\Delta H_{0,\text{rxn}} = 59 \text{ kJ mol}^{-1}$ (Table 2). Transition states for N-7-H bond dissociations, TS1-TS4, were found at 94-106 kJ mol⁻¹ relative to 2a^{+•} (Table 2). The dissociating bonds showed a moderate N-7···H separation in TS1 and TS2, 1.492 and 1.477 Å, respectively (Scheme 2), and similarly for TS3 and TS4 (Scheme S2). The conformationally optimized structures of TS1-TS4 revealed substantial changes in the side chain folding compared to those in $2a^{+\bullet}$ and $2b^{+\bullet}$. In general, reaching the TS was associated with a side-chain unfolding away

from the imidazole ring, regardless of the *syn-* or *anti-*facial position of the departing hydrogen atom. The N-7–H bond dissociation led to the formation of a weak complex of the H atom with the guanosine conjugate, as represented by $2j^{+\bullet}$ and $2k^{+\bullet}$ (Scheme 2). The conformational diversity of TS1–TS4, as well as their similar energies, indicated that there may be multiple transition states for the N-7-H loss, converging to conformers of the reaction product 3^+ .

The dissociation by loss of guanine (Scheme 3) was calculated to produce ion 4^{+•} and the N-7-H tautomer of neutral guanine at a very low threshold energy (46 kJ mol⁻¹, Table 2), which was further reduced for the calculated free energy change because of the gain of rotational and translational entropy of the products, resulting in an exoergic dissociation ($\Delta G_{\text{rxn},310} = -13 \text{ kJ mol}^{-1}$) overall. Because of the protonation pattern in 2a+• the neutral guanine molecule was formed as the most stable N-7-H tautomer.³⁹⁻⁴¹ Investigation of the dissociation pathway for the loss of guanine revealed multiple transition states differing in the side-chain conformation. The lowest energy TS5 was 97 kJ mol⁻¹ relative to 2a^{+•} (Table 2) and was stabilized by hydrogen bonding between the side-chain carbamate and guanine NH2 groups (Scheme 3). The separation of N-9 and C-1' in TS5 was remarkably small (1.872 Å, Scheme 3), indicating a bond elongation of only 0.43 Å (30%) in an early transition state. Accordingly, the N-9-C-1' bond dissociation was exoergic, forming an ion-molecule complex $(2l^{+\bullet})$, which was at -13 kJ mol^{-1} relative to $2a^{+\bullet}$ at 0 K.

We used the lowest energy **TS1** for transition-state-theory calculations of the thermal rate constant for the loss of H from $2\mathbf{a}^{+\bullet}$ and $2\mathbf{b}^{+\bullet}$ ($k_{\rm H}$). The calculated $k_{\rm H}$, as well as the rate constant for the guanine loss ($k_{\rm guan}$), bracketed the experimental rate constants in the same narrow interval of temperatures of 340–355 K (Figure S9), which were consistent with the typical effective temperatures of ions stored in ion traps. The

Scheme 3. Loss of Guanine from Conjugate 2a+•a

^aRelative 0 K energies in kJ mol⁻¹ in parentheses.

calculated rate constant ratio in this temperature interval, $k_{\rm guan}/k_{\rm H}=0.079-0.099$, was close to the experimental ratio (0.077–0.096). However, TST calculations yielded lower rate constants for the loss of D from D₇-2a^{+•}, thus indicating a substantial regular isotope effect (Figure S9). This computational result chiefly followed from the standard zero-point energy effect of D substitution that increased the energy of D₇-TS1 relative to D₇-2a^{+•} from 94 to 105 kJ mol⁻¹ (Table 2). We note that the calculated ratios of partition functions for the TS1 and reactants at 350 K were $Q^{\ddagger}/Q=2.28$ and 2.76 for TS1/2a^{+•} and D₇-TS1/D₇-2a^{+•}, respectively, favoring D₇-TS1 by about 20%. However, this small enhancement was insufficient to overcome the much larger effect of increased activation energy.

Inverse isotope effects are usually explained by an isotopedependent coupled equilibrium that prefers the labeled form (equilibrium isotope effect). 46-49 We examined a possible equilibration of 2a+ involving a H-7 or D-7 transfer to an adjacent position. A 1,2-migration of H-7 to C-8 would form ion $2g^{+\bullet}$ (Scheme S2) which was substantially more stable than $2a^{+\bullet}$ (Table 2). However, formation of $2g^{+\bullet}$ as an intermediate would have increased the barrier for H loss to 124 kJ mol⁻¹, which was inconsistent with the rapid kinetics of H/D ejection. Moreover, loss of both D and H should be expected had $2g^{+\bullet}$ been an intermediate, in stark contrast with the experimental results for the spontaneous dissociation. 1,2-Hydrogen atom migration to C-5 would form isomer 2i^{+•} of comparable energy as 2a^{+•}. However, attempts to locate the TS for the 1,2-H migration resulted in dissociation, making 2i++ and another low-energy isomer (2h+•) kinetically inaccessible from 2a+•. A tentative explanation of the isotope-effect discrepancy between experiment and TST theory can be invoked from the properties of the potential energy surface post-TS1. The departing hydrogen atom can be temporarily retained in a complex (2k+* or 2j+*,

Scheme 2), which was calculated to be a potential energy minimum in equilibrium with 2a^{+•} or 2b^{+•}. Complex 2j^{+•} was isoenergetic with the products (both at 59 kJ mol⁻¹ relative to 2a^{+•}, Table 2), which was due to a stabilizing refolding of the side chain in 3+ which must have involved a free- energy barrier (Scheme 2). Similarly, complex $2k^{+\bullet}$, which was a local energy minimum but above the lowest energy products, owed its existence to a side-chain conformation change on the route to 3⁺ that was associated with a free-energy barrier. Unfortunately, calculating these energy barriers turned out to be very demanding and we did not pursue it. Importantly, the reverse H···N-7 recombination in $2k^{+\bullet}$ was calculated to be 5.7 fold faster at 350 K than the D···N-7 recombination in D_7 -2 $k^{+\bullet}$. Thus, if the overall dynamics of the loss of H and D from complexes 2j⁺ or 2k⁺ and their D₇-isotopologues preferred the departure of the heavier isotope, the inverse isotope effect could be attributed to an isotope-dependent coupled equilibrium involving H-atom complexes with the conformers of product ion 3⁺. This could be investigated by all-electron molecular dynamics starting from the transition state and including vibrationally excited H-atom complexes. However, because of the open-shell nature of the system and relatively small variations of the potential energy surface, such calculations would require an ab initio Hamiltonian and a basis set of good quality to capture the dissociation kinetics, which is beyond the scope of the present work.

4. CONCLUSIONS

Elusive guanosine radicals representing hydrogen atom adducts to guanine, $(G + H)^{\bullet}$, were generated for the first time in the gas phase in the form of conjugates carrying a fixed-charge trialkylammonium group. The successful generation necessi-

tated an indirect approach, consisting of electron transfer dissociation of a noncovalent crown-ether complexes of the doubly charged conjugates. This technique appears to be generally applicable to forming fragile biomolecular radicals in the gas phase. The charged tag was transparent in the 210-700 nm range, and its absorption did not interfere with that of the nucleoside radical that can be studied by ion action spectroscopy. Charge-tagged guanosine radicals represent a case of transient intermediates that are susceptible to spontaneous dissociation that makes them a challenging target for experimental studies. At the same time, the conformational flexibility of the charged tag requires Born-Oppenheimer molecular dynamics to adequately treat the ion thermodynamics and obtain conformationally optimized transition states. Despite these difficulties, we were able to spectroscopically characterize the ions as being guanosine N-7-H radical tautomers. The absorption bands in the visible and near-UV regions of the spectrum were found to be characteristic of guanosine radicals of this position-specific (G + H) type while distinguishing them from other radical protomers. This UV-vis absorption characteristic can be used to identify guanine radicals in more complex guanine-containing oligonucleotide and DNA radicals of relevance for DNA damage. The guanine radical dissociations were found to display a large inverse isotope effect on the spontaneous loss of H. Accurate treatment of this effect using ab initio molecular dynamics appears to be necessary to explain this interesting observation.

ASSOCIATED CONTENT

Supporting Information

The Supporting Information is available free of charge at https://pubs.acs.org/doi/10.1021/jasms.0c00459.

Description of synthetic procedures, compound characterization, auxiliary figures of mass spectra, TST calculations and discussion of kinetics, molecular orbitals, UV—vis action spectra of cations, and TD-DFT calculated absorption spectra (PDF)

AUTHOR INFORMATION

Corresponding Authors

František Tureček — Department of Chemistry, Bagley Hall, Box 351700, University of Washington, Seattle, Washington 98195-1700, United States; Institute of Organic Chemistry and Biochemistry, Czech Academy of Sciences, 16610 Prague 6, Czech Republic; orcid.org/0000-0001-7321-7858; Phone: +1-206-685-2041l; Email: turecek@uw.edu

Aleš Marek — Institute of Organic Chemistry and Biochemistry, Czech Academy of Sciences, 16610 Prague 6, Czech Republic; Email: ales.marek@uochb.cas.cz

Authors

Yue Liu — Department of Chemistry, Bagley Hall, Box 351700, University of Washington, Seattle, Washington 98195-1700, United States

Congcong Ma – Department of Chemistry, Bagley Hall, Box 351700, University of Washington, Seattle, Washington 98195-1700, United States

Calvin J. A. Leonen – Department of Chemistry, Bagley Hall, Box 351700, University of Washington, Seattle, Washington 98195-1700, United States

- Champak Chatterjee Department of Chemistry, Bagley Hall, Box 351700, University of Washington, Seattle, Washington 98195-1700, United States
- Gabriela Nováková Institute of Organic Chemistry and Biochemistry, Czech Academy of Sciences, 16610 Prague 6, Czech Republic

Complete contact information is available at: https://pubs.acs.org/10.1021/jasms.0c00459

Notes

The authors declare no competing financial interest.

ACKNOWLEDGMENTS

Research at the University of Washington was supported by the Chemistry Division of the U.S. National Science Foundation, Grants CHE-1951518 for experimental work and CHE-1661815 for computations. C.C. acknowledges support from NIH R01GM110430 and NSF MCB 1715123. F.T. acknowledges support by the Klaus and Mary Ann Saegebarth Endowment. Research at the IOCB was supported by the Ministry of Education, Youth and Sport (MSMT INTER-EXCELLENCE LTAUSA19094).

REFERENCES

- (1) Dougherty, D.; Younathan, E. S.; Voll, R.; Abdulnur, S.; McGlynn, S. P. Photoelectron Spectroscopy of Some Biological Molecules. *J. Electron Spectrosc. Relat. Phenom.* **1978**, *13*, 370–393.
- (2) Xie, H.; Yang, D.; Heller, A.; Gao, Z. Electrocatalytic Oxidation of Guanine, Guanosine, and Guanosine Monophosphate. *Biophys. J.* **2007**, 92, L70–L72.
- (3) Seidel, C. A. M.; Schulz, A.; Sauer, M. H. M. Nucleobase-Specific Quenching of Fluorescent Dyes. 1. Nucleobase One-Electron Redox Potentials and Their Correlation with Static and Dynamic Quenching Efficiencies. *J. Phys. Chem.* **1996**, *100*, 5541–5553.
- (4) Steenken, S.; Jovanovic, S. V. How Easily Oxidizable Is DNA? One-Electron Reduction Potentials of Adenosine and Guanosine Radicals in Aqueous Solution. *J. Am. Chem. Soc.* **1997**, *119*, 617–618.
- (5) Kanvah, S.; Joseph, J.; Schuster, G. B.; Barnett, R. N.; Cleveland, C. L.; Landman, U. Oxidation of DNA: Damage to Nucleobases. *Acc. Chem. Res.* **2010**, *43*, 280–287.
- (6) Kino, K.; Hirao-Suzuki, M.; Morikawa, M.; Sakaga, A.; Miyazawa, H. Generation, Repair and Replication of Guanine Oxidation Products. *Genes Environ.* **2017**, *39*, 21.
- (7) Szyperska, A.; Rak, J.; Leszczynski, J.; Li, X.; Ko, Y. J.; Wang, H.; Bowen, K. H. Valence Anions of 9-Methylguanine-1-Methylcytosine Complexes. Computational and Photoelectron Spectroscopy Studies. *J. Am. Chem. Soc.* **2009**, *131*, 2663–2669.
- (8) Chen, H.-Y.; Kao, C.-L.; Hsu, S. C. N. Proton Transfer in Guanine-Cytosine Radical Anion Embedded in B-Form DNA. *J. Am. Chem. Soc.* **2009**, *131*, 15930–15938.
- (9) Liu, Y.; Korn, J. A.; Dang, A.; Turecek, F. Hydrogen-Rich Cation Radicals of DNA Dinucleotides. Generation and Structure Elucidation by UV-Vis Action Spectroscopy. *J. Phys. Chem. B* **2018**, 122, 9665–9680.
- (10) Coon, J. J.; Ueberheide, B.; Syka, J. E. P.; Dryhurst, D. D.; Ausio, J.; Shabanowitz, J.; Hunt, D. F. Protein Identification Using Sequential Ion/Ion Reactions and Tandem Mass Spectrometry. *Proc. Natl. Acad. Sci. U. S. A.* **2005**, *102*, 9463–9468.
- (11) Shaffer, S. A.; Tureček, F. A Marginally Stable Hypervalent Radical. J. Am. Chem. Soc. 1994, 116, 8647–8653.
- (12) Frøsig, L.; Tureček, F. Hypervalent Pyrrolidinium Radicals by Neutralization-Reionization Mass Spectrometry. Metastability and Radical Leaving Group Abilities. *J. Am. Soc. Mass Spectrom.* **1998**, *9*, 242–254.
- (13) Dang, A.; Korn, J. A.; Gladden, J.; Mozzone, B.; Tureček, F. UV-Vis Photodissociation Action Spectroscopy on Thermo LTQ-XL ETD

- and Bruker amaZon Ion Trap Mass Spectrometers: A Practical Guide. J. Am. Soc. Mass Spectrom. 2019, 30, 1558–1564.
- (14) Shaffer, C. J.; Andrikopoulos, P. C.; Řezáč, J.; Rulíšek, L.; Tureček, F. Efficient Covalent Bond Formation in Gas-Phase Peptide-Peptide Ion Complexes with the Photoleucine Stapler. *J. Am. Soc. Mass Spectrom.* **2016**, 27, 633–645.
- (15) Nguyen, H. T. H.; Andrikopoulos, P. C.; Bím, D.; Rulíšek, L.; Dang, A.; Tureček, F. Radical Reactions Affecting Polar Groups in Threonine Peptide Ions. *J. Phys. Chem. B* **2017**, *121*, 6557–6569.
- (16) Řezáč, J.; Fanfrlík, J.; Salahub, D.; Hobza, P. Semi-Empirical Quantum Chemical PM6Method Augmented by Dispersion and H Bonding Correction Terms Reliably Describes Various Types of Noncovalent Complexes. J. Chem. Theory Comput. 2009, 5, 1749–1760.
- (17) Berendsen, H. J.; Postma, J. V.; van Gunsteren, W. F.; DiNola, A. R. H. J.; Haak, J. R. Molecular Dynamics with Coupling to an External Bath. *J. Chem. Phys.* **1984**, *81*, 3684–3690.
- (18) Řezáč, J. Cuby: An Integrative Framework for Computational Chemistry. *J. Comput. Chem.* **2016**, 37, 1230–1237.
- (19) Stewart, J. J. P. MOPAC 16. Stewart Computational Chemistry; Colorado Springs, CO, 2016.
- (20) Becke, A. D. Density-Functional Exchange-Energy Approximation with Correct Asymptotic Behavior. *Phys. Rev. A: At., Mol., Opt. Phys.* **1988**, *38*, 3098–3100.
- (21) Robb, M. A.; Cheeseman, J. R.; Scalmani, G.; Barone, V.; Petersson, G. A.; Nakatsuji, H.; Caricato, M.; Marenich, A. V.; Bloino, J.; Janesko, B. G.; Gomperts, R.; Mennucci, B.; Hratchian, H. P.; Ortiz, J. V.; Izmaylov, A. F.; Sonnenberg, J. L.; Williams-Young, D.; Ding, F.; Lipparini, F.; Egidi, F.; Goings, J.; Peng, B.; Petrone, A.; Henderson, T.; Ranasinghe, D.; Zakrzewski, V. G.; Gao, J.; Rega, N.; Zheng, G.; Liang, W.; Hada, M.; Ehara, M.; Toyota, K.; Fukuda, R.; Hasegawa, J.; Ishida, M.; Nakajima, T.; Honda, Y.; Kitao, O.; Nakai, H.; Vreven, T.; Throssell, K.; Montgomery, J. A., Jr.; Peralta, J. E.; Ogliaro, F.; Bearpark, M. J.; Heyd, J. J.; Brothers, E. N.; Kudin, K. N.; Staroverov, V. N.; Keith, T. A.; Kobayashi, R.; Normand, J.; Raghavachari, K.; Rendell, A. P.; Burant, J. C.; Iyengar, S. S.; Tomasi, J.; Cossi, M.; Millam, J. M.; Klene, M.; Adamo, C.; Cammi, R.; Ochterski, J. W.; Martin, R. L.; Morokuma, K.; Farkas, O.; Foresman, J. B.; Fox, D. J. Gaussian 16, Revision A03; Gaussian, Inc.: Wallingford, CT, 2016.
- (22) McClurg, R. B.; Flagan, R. C.; Goddard, W. A., III The Hindered Rotor Density-of-States Interpolation Function. *J. Chem. Phys.* **1997**, 106, 6675–6680.
- (23) Zhao, Y.; Truhlar, D. G. The M06 Suite of Density Functionals for Main Group Thermochemistry, Thermochemical Kinetics, Noncovalent Interactions, Excited States, and Transition Elements: Two New Functionals and Systematic Testing of Four M06-Class Functionals and 12 Other Functionals. *Theor. Chem. Acc.* 2008, 120, 215—241
- (24) Furche, F.; Ahlrichs, R. Adiabatic Time-Dependent Density Functional Methods for Excited State Properties. *J. Chem. Phys.* **2002**, 117, 7433–7447.
- (25) Huang, S. R.; Tureček, F. Cation Radicals of Hachimoji Nucleobases. Canonical Purine and Noncanonical Pyrimidine Forms Generated in the Gas Phase and Characterized by UV-Vis Photodissociation Action Spectroscopy. *J. Phys. Chem. A* **2020**, *124*, 7101–7112.
- (26) Huang, S. R.; Dang, A.; Tureček, F. Ground and Excited States of Gas-Phase DNA Nucleobase Cation-Radicals. A UV-Vis Photodisociation Action Spectroscopy and Computational Study of Adenine and 9-Methyladenine. J. Am. Soc. Mass Spectrom. 2020, 31, 1271–1281.
- (27) Comeau, D. C.; Bartlett, R. J. The Equation-of-Motion Coupled-Cluster Method. Applications to Open- and Closed-Shell Reference States. *Chem. Phys. Lett.* **1993**, 207, 414–423.
- (28) Wigner, E. The Quantum Correction for Thermodynamic Equilibrium. *Phys. Rev.* **1932**, *40*, 749–759.
- (29) Bonacic-Koutecky, V.; Mitric, R. Theoretical Exploration of Ultrafast Dynamics in Atomic Clusters: Analysis and Control. *Chem. Rev.* **2005**, *105*, 11–65.
- (30) Barbatti, M.; Ruckenbauer, M.; Plasser, F.; Pittner, J.; Granucci, G.; Persico, M.; Lischka, H. Newton-X: A Surface-Hopping Program for

- Nonadiabatic Molecular Dynamics. Wiley Interdiscip. Rev. Comput. Mol. Sci. 2014, 4, 26–33.
- (31) Korn, J. A.; Urban, J.; Dang, A.; Nguyen, H. T. H.; Turecek, F. UV-Vis Action Spectroscopy Reveals a Conformational Collapse in Hydrogen-Rich Dinucleotide Cation Radicals. *J. Phys. Chem. Lett.* **2017**, 8, 4100–4107.
- (32) Liu, Y.; Dang, A.; Urban, J.; Tureček, F. Charge-Tagged DNA Radicals in the Gas Phase Characterized by UV-Vis Photodissociation Action Spectroscopy. *Angew. Chem., Int. Ed.* **2020**, *59*, 7772–7777.
- (33) McClellan, J. E.; Murphy III, J. P.; Mulholland, J. J.; Yost, R. A. Effects of Fragile Ions on Mass Resolution and on Isolation for Tandem Mass Spectrometry in the Quadrupole Ion Trap Mass Spectrometer. *Anal. Chem.* **2002**, *74*, 402–412.
- (34) Swaney, D. L.; McAlister, G. C.; Wirtala, M.; Schwartz, J. C.; Syka, J. E. P.; Coon, J. J. Supplemental Activation Method for Highly Efficient Electron Transfer Dissociation of Doubly Protonated Peptide Precursors. *Anal. Chem.* **2007**, *79*, 477–485.
- (35) Pepin, R.; Layton, E. D.; Liu, Y.; Afonso, C.; Tureček, F. Where Does the Electron Go? Stable and Metastable Peptide Cation Radicals Formed by Electron Transfer. *J. Am. Soc. Mass Spectrom.* **2017**, 28, 164–181.
- (36) Colominas, C.; Luque, F. J.; Orozco, M. Tautomerism and Protonation of Guanine and Cytosine. Implications in the Formation of Hydrogen-Bonded Complexes. *J. Am. Chem. Soc.* **1996**, *118*, 6811–6821.
- (37) Halder, A.; Bhattacharya, S.; Datta, A.; Bhattacharyya, D.; Mitra, A. The Role of N7 Protonation of Guanine in Determining the Structure, Stability and Function of RNA Base Pairs. *Phys. Chem. Chem. Phys.* **2015**, *17*, 26249–26263.
- (38) Wu, R. R.; Yang, B.; Berden, G.; Oomens, J.; Rodgers, M. T. Gas-Phase Conformations and Energetics of Protonated 2-Deoxyguanosine and Guanosine: IRMPD Action Spectroscopy and Theoretical Studies. *J. Phys. Chem. B* **2014**, *118*, 14774—14784.
- (39) Karton, A. Thermochemistry of Guanine Tautomers Re-Examined by Means of High-Level CCSD(T) Composite Ab Initio Methods. *Aust. J. Chem.* **2019**, *72*, 607–613.
- (40) Hanus, M.; Ryjacek, F.; Kabelac, M.; Kubar, T.; Bogdan, T. V.; Trygubenko, S. A.; Hobza, P. Correlated ab Initio Study of Nucleic Acid Bases and Their Tautomers in the Gas Phase, in a Microhydrated Environment and in Aqueous Solution. Guanine: Surprising Stabilization of Rare Tautomers in Aqueous Solution. *J. Am. Chem. Soc.* 2003, 125, 7678–7688.
- (41) Sponer, J.; Hobza, P. Molecular Interactions of Nucleic Acid Bases. A Review of Quantum-Chemical Studies. *Collect. Czech. Chem. Commun.* **2003**, *68*, 2231–2282.
- (42) Goeringer, D. E.; McLuckey, S. A. Evolution of Ion Internal Energy during Collisional Excitation in the Paul Ion Trap: A Stochastic Approach. *J. Chem. Phys.* **1996**, *104*, 2214–2221.
- (43) Gronert, S. Estimation of Effective Ion Temperatures in a Quadrupole Ion Trap. J. Am. Soc. Mass Spectrom. 1998, 9, 845–848.
- (44) Lovejoy, E. R.; Wilson, R. R. Kinetic Studies of Negative Ion Reactions in a Quadrupole Ion Trap: Absolute Rate Coefficients and Ion Energies. *J. Phys. Chem. A* **1998**, *102*, 2309–2315.
- (45) Donald, W. A.; Khairallah, G. N.; O'Hair, R. A. J. The Effective Temperature of Ions Stored in a Linear Quadrupole Ion Trap Mass Spectrometer. *J. Am. Soc. Mass Spectrom.* **2013**, 24, 811–815.
- (46) Parkin, G. Temperature-Dependent Transitions Betweem Normal and Inverse Isotope Effects Pertaining to the Interaction of H-H and C-H Bonds with Transition Metal Centers. *Acc. Chem. Res.* **2009**, *42*, 315–325.
- (47) Cheng, T. Y.; Bullock, R. M. Isotope Effects on Hydride Transfer Reactions from Transition Metal Hydrides to Trityl Cation. An Inverse Isotope Effect for a Hydride Transfer. *J. Am. Chem. Soc.* **1999**, *121*, 3150–3155.
- (48) Jones, W. D. Isotope Effects in C-H Bond Activation Reactions by Transition Metals. *Acc. Chem. Res.* **2003**, *36*, 140–146.
- (49) Petralia, L. S.; Tsikritea, A.; Loreau, J.; Softley, T. P.; Heazlewood, B. R. Strong Inverse Kinetic Isotope Effect Observed in Ammonia Charge Exchange Reactions. *Nat. Commun.* **2020**, *11*, 173.